Chinese Chemical Letters 35 (2024) 109462

Contents lists available at ScienceDirect

Chinese Chemical Letters

journal homepage: www.elsevier.com/locate/cclet

Efficient tunable visible and near-infrared emission in Sb^{3+}/Sm^{3+}-codoped $Cs_2NaLuCl_6$ for near-infrared light-emitting diode, triple-mode fluorescence anti-counterfeiting and information encryption

Hui Peng[a,*], Xiao Wang[a], Weiguo Huang[a], Shuiyue Yu[a], Linghang Kong[a], Qilin Wei[b,*], Jialong Zhao[a], Bingsuo Zou[a,*]

[a] State Key Laboratory of Featured Metal Materials and Life-cycle Safety for Composite Structures, MOE Key Laboratory of New Processing Technology for Nonferrous Metals and Materials, and School of Resources, Environment and Materials, Guangxi University, Nanning 530004, China
[b] School of Chemistry and Chemical Engineering, Shandong University, Ji'nan 250100, China

ARTICLE INFO

Article history:
Received 2 December 2023
Revised 19 December 2023
Accepted 26 December 2023
Available online 6 January 2024

Keywords:
Rare earth-based double perovskites
Self-trapped exciton
Near-infrared emission
Energy transfer
Multifunctional applications

ABSTRACT

Rare earth ions (RE^{3+})-doped double perovskites have attracted tremendous attention for its fascinating optical properties. Nevertheless, RE^{3+} generally exhibits poor photoluminescence quantum yield (PLQY) for their parity-forbidden 4f-4f transition and the low doping concentration. Herein, we reported Sb^{3+}/Sm^{3+}-codoped rare earth-based double perovskite $Cs_2NaLuCl_6$ that enables efficient visible and near-infrared (NIR) emission, which stems from self-trapped exciton (STE) and Sm^{3+}, respectively. Benefit from up to 72.89% energy transfer efficiency from STE to Sm^{3+} and high doping concentrations due to similar ionic activity between Sm^{3+} and Lu^{3+}, thus eruptive PLQY of 74.58% in the visible light region and 23.12% in the NIR light region can be obtained. Moreover, Sb^{3+}/Sm^{3+}-codoped $Cs_2NaLuCl_6$ exhibits tunable emission characteristic in the visible light region under different excitation wavelengths, which can change from blue emission (254 nm excitation) to white emission (365 nm excitation). More particularly, only the NIR emission can be captured by the NIR camera when a 700 nm cutoff filter is added. The excellent stability and unique optical properties of Sb^{3+}/Sm^{3+}-codoped $Cs_2NaLuCl_6$ enable us to demonstrate its applications in NIR light-emitting diode, triple-mode fluorescence anti-counterfeiting and information encryption. These findings provide new inspiration for the application of rare earth-based double perovskite in optoelectronic devices.

Lead halide perovskites (LHPs) have shown broad applications in lighting, display, and biological imaging due to their fascinating optical properties and ease of synthesis [1,2]. However, the current study was mainly limited to the visible light region. To expand the application range of LHPs, some rare earth ions (RE^{3+}) singly-doped LPHs with NIR emission have been reported. In this regard, a typical example is that the PLQY of Yb^{3+} singly-doped $CsPbCl_3$ can over 100% through quantum cutting [3]. Although the initial achievements have been made, the intrinsic toxicity of lead and the poor stability of LHPs severely limit its further application.

Lead-free double perovskites (DPs), with the formula of $Cs_2A^IB^{III}Cl_6$ (A = Na, K, Ag, Cu; B = In, Bi, Sb), have drawn much attention due to their low toxicity and unique photoelectric properties, and it is considered as an ideal alternative to LPHs [4–6]. However, RE^{3+} singly-doped DPs generally show the poor NIR emission intensity (*e.g.*, Yb^{3+} singly-doped $Cs_2AgInCl_6$ [7] and Ho^{3+} singly-doped Cs_2KInCl_6 [8]), which cannot meet the needs of practical application. To alleviate this, the introduction of metal ion sensitizers into RE^{3+}-doped DPs can effectively boost the emission intensity of RE^{3+} *via* the energy transfer (ET) from sensitizers to RE^{3+}. Among various schemes, ns^2 metal ions (Sb^{3+} and Bi^{3+}) and RE^{3+}-codoped DPs have been demonstrated to be a feasible strategy [9–11], as they have the same valence state and similar ion radii. For example, Nag *et al.* reported Sb^{3+}/Er^{3+}-codoped $Cs_2NaInCl_6$, and the emission stems from the 4f-4f transition of Er^{3+} was greatly enhanced *via* the ET from STE to Er^{3+} [12]. Parallelly, the NIR emission of Bi^{3+}/Yb^{3+}-codoped $Cs_2AgInCl_6$ is ~27 times higher than that of the Er^{3+} singly doping [13]. However, the

* Corresponding authors.
E-mail addresses: penghuimaterial@163.com (H. Peng), qlwei@sdu.edu.cn (Q. Wei), zoubs@gxu.edu.cn (B. Zou).

https://doi.org/10.1016/j.cclet.2023.109462
1001-8417/

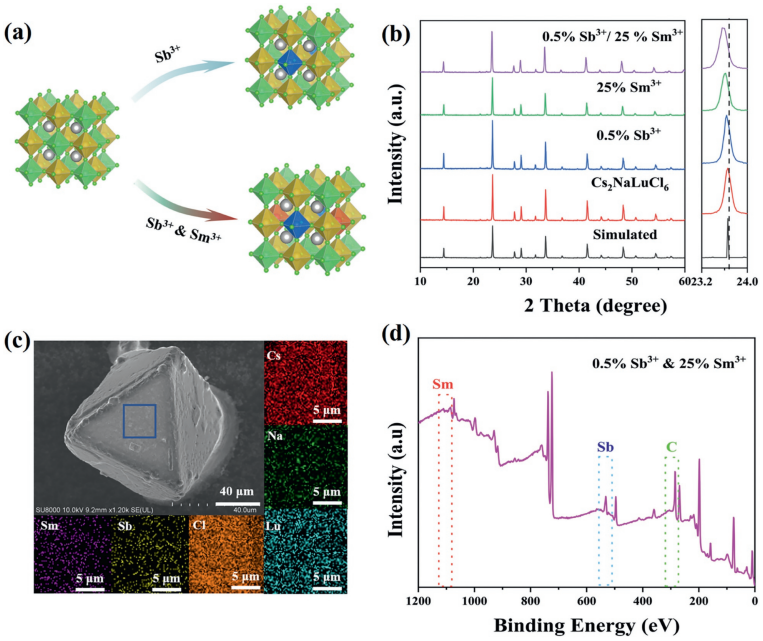

Fig. 1. (a) Crystal structure of pure $Cs_2NaLuCl_6$, Sb^{3+} singly-doped, Sm^{3+} singly-doped, and Sb^{3+}/Sm^{3+}-codoped samples. (b) XRD patterns of the as-synthesized samples. (c) SEM image and element mapping of 0.5%Sb^{3+}/25%Sm^{3+}-codoped $Cs_2NaLuCl_6$. (d) XPS of 0.5%Sb^{3+}/25%Sm^{3+}-codoped $Cs_2NaLuCl_6$ powders.

low PLQY of ns^2 metal ions and RE^{3+}-codoped DPs is still at a low level, as there is a significant difference in ionic activity between RE^{3+} and trivalent metal ions (B^{III}) of DPs, which makes it difficult for RE^{3+} to enter the host lattice and achieve efficient NIR emission. To overcome the problems, it is important to explore the rare earth-based DPs host matrix to achieve controllable RE^{3+} doping and efficient NIR emission [14].

Here, we synthesized Sb^{3+}/Sm^{3+}-codoped the carefully selected host matrix of rare earth-based $Cs_2NaLuCl_6$ DPs *via* a typical one-pot hydrothermal method. Upon photoexcitation, the fingerprint emission bands of STE emission and 4f-4f transition of Sm^{3+} in Sb^{3+}/Sm^{3+}-codoped $Cs_2NaLuCl_6$ can be witnessed, and the PLQY in the visible light region and NIR light region can reach up to 74.58% and 23.12%, respectively. The ET mechanism between STE and Sm^{3+} was discussed *via* the steady-state/transient PL spectra and temperature-dependent PL spectra. In addition, the high-performance NIR pc-LED was fabricated by coating the Sb^{3+}/Sm^{3+}-codoped $Cs_2NaLuCl_6$ powders on a 315 nm UV chip, and its diverse applications in night-vision and biomedical imaging were demonstrated. Parallelly, Sb^{3+}/Sm^{3+}-codoped $Cs_2NaLuCl_6$ also shows the excitation wavelength-dependent emission characteristics due to this compound has two different emission centers, which can change from blue emission under 254 nm excitation to white emission upon 365 nm excitation. More particularly, the visible light emission can be removed when a 700 nm cutoff filter is added, and only the NIR emission can be captured by the NIR camera. Thereby, we can construct a triple-mode optical anti-counterfeiting and information encryption based on Sb^{3+}/Sm^{3+}-codoped $Cs_2NaLuCl_6$ under various external stimuli.

All the samples were synthesized *via* a typical hydrothermal method, and more details can be found in Supporting information. Fig. 1a shows the crystal structure of $Cs_2NaLuCl_6$, which crystallizes in cubic $Fm\bar{3}m$ space group. In the Sb^{3+}/Sm^{3+}-codoped $Cs_2NaLuCl_6$, the $[SbCl_6]^{3-}$ and $[SmCl_6]^{3-}$ can partially replace $[LuCl_6]^{3-}$ in the host lattice due to their same valence state and similar coordination characteristics [8,15]. Moreover, the doped samples have similar XRD patterns with the pristine one, suggesting all the as-synthesized samples retain the $Cs_2NaLuCl_6$ structure (Fig. 1b). Compared with the pure $Cs_2NaLuCl_6$, the diffraction peak of Sb^{3+} singly-doped compound remains unchanged, which should be the low doping concentration. In stark contrast, the diffraction peak of Sm^{3+} singly-doped and Sb^{3+}/Sm^{3+}-codoped samples shifts towards to low angle. This can be attributed to the lattice expansion due to the ion radius of Sm^{3+} (90 pm, CN = 6) is larger than that of Lu^{3+} (86 pm, CN = 6) as well as the high doping content of Sm^{3+} [16]. Fig. 1c shows the SEM image of the as-synthesized Sb^{3+}/Sm^{3+}-codoped $Cs_2NaLuCl_6$. Clearly, the crystal exhibits a regular octahedral structure, which illustrates Sb^{3+}/Sm^{3+}-codoped $Cs_2NaLuCl_6$ has high crystal quality and lays the foundation for further investigation of its photophysical properties. The element mapping results illustrate that the elements of Cs, Na, Lu, Cl, Sb, and Sm are uniformly distributed on the crystal. Parallelly, the EDS result illustrates that Sb^{3+} and Sm^{3+} have doped into $Cs_2NaLuCl_6$ (Fig. S1 and Table S1 in Supporting information), and the actual doping content of Sm^{3+} is much higher than recently reported other Ln^{3+} singly-doped DPs (*e.g.*, $Cs_2AgInCl_6$ [17] and $Cs_2NaBiCl_6$ [18]) due to Sm^{3+} and Lu^{3+} have similar ionic activity. Fig. 1d depicts the XPS spectrum of Sb^{3+}/Sm^{3+}-codoped $Cs_2NaLuCl_6$, and the fingerprint bands of Sb^{3+} and Sm^{3+} are observed, which confirms the dopants are indeed doped in the host lattice.

Then, the optical properties of the as-synthesized compounds were investigated. For pure $Cs_2NaLuCl_6$, it exhibits broad blue emission (Fig. S2 in Supporting information). After Sb^{3+} doping, the blue emission intensity is greatly improved, which should be attributed to the dopant induced STE in the $[SbCl_6]^{3-}$ octahedron [19]. To demonstrates this, the excitation wavelength-dependent PL spectra were measured, and they show the similar spectral characteristics (Fig. S3a in Supporting information), and parallelly, the PLE spectra monitored at various emission wavelengths also exhibit identical profiles (Fig. S3b in Supporting information). Hence, the observed blue emission in Sb^{3+}-doped $Cs_2NaLuCl_6$ stems from the same excited state. Moreover, Sb^{3+}-doped $Cs_2NaLuCl_6$ also have a large Stokes shift of 138 nm, broad full width at half-maximum (FWHM) of 76 nm, and a long decay lifetime of 1.16 μs. Hence, we can attribute the broadband blue emission in Sb^{3+}-doped $Cs_2NaLuCl_6$ to STEs [12,13]. Fig. S4 (Supporting information) shows the PL spectra with different Sb^{3+} doping concentrations. Clearly, the strongest emission for Sb^{3+} singly-doped $Cs_2NaLuCl_6$

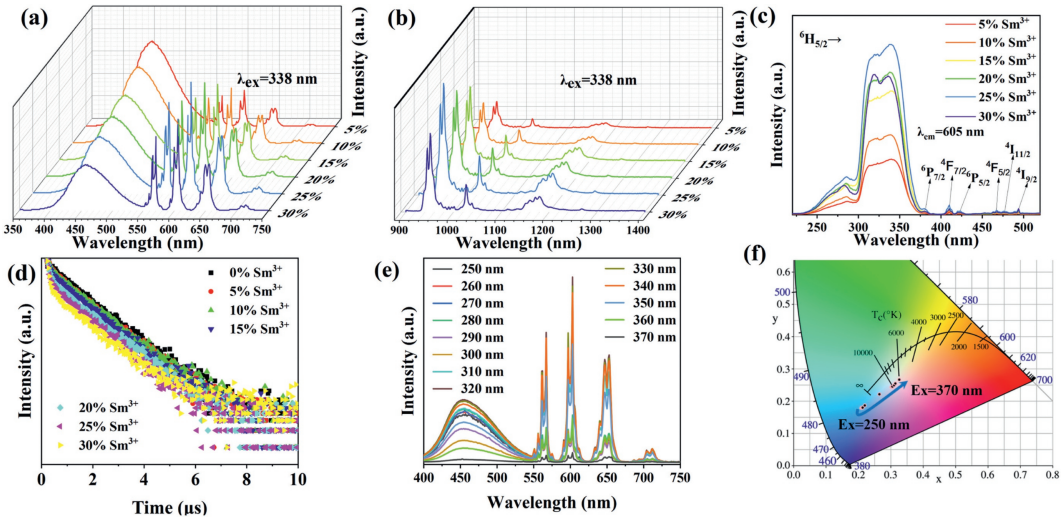

Fig. 2. PL spectra of Sb^{3+}/Sm^{3+}-codoped $Cs_2NaLuCl_6$ with various Sm^{3+} doping concentrations in (a) visible light region and (b) NIR light region (excited at 338 nm). (c) PLE spectra of Sb^{3+}/Sm^{3+}-codoped $Cs_2NaLuCl_6$ monitored at 605 nm. (d) PL decay lifetime of Sb^{3+}/Sm^{3+}-codoped $Cs_2NaLuCl_6$ monitored at 456 nm (STE emission band) under 320 nm laser excitation. (e) PL spectra of 0.5%Sb^{3+}/20%Sm^{3+}-codoped $Cs_2NaLuCl_6$ under various excitation wavelengths (250-370 nm). (f) CIE color coordinates of 0.5%Sb^{3+}/20%Sm^{3+}-codoped $Cs_2NaLuCl_6$.

can be obtained when the feed content of Sb^{3+} is 0.5%, and the corresponding PLQY is 98% and the PL decay lifetime is 1.16 μs. Fig. S5 (Supporting information) shows the PLE spectra of Sb^{3+} singly-doped $Cs_2NaLuCl_6$, and three different excitation bands at 267, 280, and 338 nm are observed, which can be assigned to the electronic transitions of $^1S_0 \rightarrow {}^1P_1$, $^1S_0 \rightarrow {}^3P_2$, and $^1S_0 \rightarrow {}^3P_1$ of Sb^{3+}, respectively [20]. Fig. S6 (Supporting information) shows the temperature-dependent emission spectra of 0.5%Sb^{3+} singly-doped $Cs_2NaLuCl_6$. Clearly, the single broad emission band can be observed within the entire testing temperature range (Fig. S6a). Moreover, the PL intensity decreases gradually with increasing of temperature, which should be attributed to the thermal quenching effect [8,21]. The exciton binding energy (E_b) was determined to be 77.7 meV (Fig. S6b), indicating that the electron-hole pair is a typical Frenkel-like exciton [22]. The Huang-Rhys factor (S) was calculated to be 20.0, which illustrates a strong electron-phonon coupling in Sb^{3+} singly-doped $Cs_2NaLuCl_6$ (Fig. S6c), which is conducive to the formation of STEs [23]. Moreover, the detailed photophysical mechanism of STE observed in Sb^{3+} singly-doped $Cs_2NaLuCl_6$ is given in Fig. S6d.

Figs. 2a and b show the PL spectra of Sb^{3+}/Sm^{3+}-codoped $Cs_2NaLuCl_6$ crystals. Clearly, the PL spectra of the codoped samples cover from visible to NIR light region. Besides the STE emission, there are multiple emission bands can be obtained, which corresponds to the $^4G_{5/2} \rightarrow {}^6H_{J\ =\ 5/2,7/2,9/2,11/2}$ (563, 605, 657, and 709 nm), $^4G_{5/2} \rightarrow {}^6F_{5/2}$ (952 nm), $^4G_{5/2} \rightarrow {}^6F_{7/2}$ (1027 nm), $^4G_{5/2} \rightarrow {}^6F_{9/2}$ (1079 nm), and $^4G_{5/2} \rightarrow {}^6F_{11/2}$ (1267 nm) transitions of Sm^{3+}, respectively. Moreover, we also synthesized Sm^{3+} singly-doped $Cs_2NaLuCl_6$, and the corresponding PL spectrum is given in Fig. S7 (Supporting information). Upon UV irradiation, the PL intensity of Sb^{3+}/Sm^{3+}-codoped $Cs_2NaLuCl_6$ is 54 times that of Sm^{3+} singly-doped $Cs_2NaLuCl_6$, which suggests that the emission intensity stems from 4f-4f transition of Sm^{3+} can be enhanced by Sb^{3+} sensitization [24]. Notably, the PL intensity of broadband STE emission decreases gradually at higher Sm^{3+} doping content, while the emission intensity stems from Sm^{3+} increases gradually with increasing of Sm^{3+} doping concentration (0-25%), which indicates a distinct ET from STE to Sm^{3+} [18]. When the doping concentration of Sm^{3+} is further increased, the luminescence intensity begins to decrease, which is caused by a typical concentration quenching effect [25,26]. Moreover, the optimal PLQY of 0.5%Sb^{3+}/25%Sm^{3+}-codoped $Cs_2NaLuCl_6$ in the visible light range is 74.58%, and more particularly, the PLQY in the NIR light region is 23.12%. Such high NIR PLQY in our system is higher than recently reported RE^{3+}-doped all-inorganic non-rare earth-based DPs (Table S2 in Supporting information), which should be attributed to the similar ionic activity between Lu^{3+} and Sm^{3+}, thus allowing more Sm^{3+} ions enter the host lattice and yields efficient NIR emission [27]. Fig. 2c shows the PLE spectra of Sb^{3+}/Sm^{3+}-codoped $Cs_2NaLuCl_6$, and the variation trend of PLE under different Sm^{3+} doping concentrations is in line with the change in PL intensity. Compared with Sb^{3+} singly-doped samples, there are additional PLE bands at 380, 410, 420, 468, 476, 494 nm in the Sb^{3+}/Sm^{3+}-codoped $Cs_2NaLuCl_6$ when monitored at 605 nm, which can be assigned to $^6H_{5/2}$-$^6P_{7/2}$, $^6H_{5/2}$-$^4F_{7/2}$, $^6H_{5/2}$-$^6P_{5/2}$, $^6H_{5/2}$-$^4F_{5/2}$, $^6H_{5/2}$-$^4I_{11/2}$, $^6H_{5/2}$-$^4I_{9/2}$ transitions of Sm^{3+} [28]. Apparently, the spectral overlap between STE emission and Sm^{3+} excitation can also be witnessed (Fig. S8 in Supporting information), illustrating the presence of Förster resonant ET from STE to Sm^{3+} [8]. Moreover, the PLE intensity below 360 nm is stronger than the intrinsic excitation bands of Sm^{3+}, which enables a stronger PL intensity *via* ET from STE to Sm^{3+} (Fig. S8). Significantly, STE and Sm^{3+} emission have clear spectral overlap (Fig. 2a), and the characteristic PLE bands of both STE and Sm^{3+} can be witnessed in the PLE spectra of Sb^{3+}/Sm^{3+}-codoped $Cs_2NaLuCl_6$ (monitored at 605 nm, Fig. 2c). Hence, the above results fully demonstrate that the efficient emission of Sm^{3+} in the Sb^{3+}/Sm^{3+}-codoped $Cs_2NaLuCl_6$ stems from the ET of STE. As we know, Sb^{3+}-induced STE emission shows a wide PLE band and intense absorption [29]. Thus, the ET from STE to Sm^{3+} can overcome the weak absorption of the forbidden 4f-4f transition and boost the PL intensity of Sm^{3+} [30]. In general, the emission of RE^{3+} with 4f-4f transition is sensitive to the excitation energy [31]. Nevertheless, the normalized PL spectra of Sb^{3+}/Sm^{3+}-codoped $Cs_2NaLuCl_6$ exhibit a similar spectral feature under 310-340 nm excitation (Fig. S9 in Supporting information). Thereby, the indirect excitation dominant excitation mechanism of Sm^{3+} in Sb^{3+}/Sm^{3+}-codoped $Cs_2NaLuCl_6$ [32].

In order to quantitatively describe the ET process from STE to Sm^{3+}, we calculated the ET efficiency using the following equation:

$$\eta_{ET} = 1 - \frac{\tau_x}{\tau_0} \quad (1)$$

where τ_0 and τ_x are the PL decay lifetime of STE without and with Sm^{3+} doping. Fig. 2d shows the PL decay lifetime of STE emission in the as-synthesized samples. For Sb^{3+} singly-doped $Cs_2NaLuCl_6$, the PL decay lifetime of STE is fitted by single-exponential function. Under influence the energy transfer from Sb^{3+} to Sm^{3+}, the PL decay lifetime of STE in Sb^{3+}/Sm^{3+}-codoped $Cs_2NaLuCl_6$ is fitted by double-exponential function. Moreover, the PL decay lifetime of STE decreases gradually with increasing of Sm^{3+} doping content (Table S3 in Supporting information), which is accompanied by the increases of ET efficiency. When the ET efficiency reaches 72.89%, the Sm^{3+} exhibits the strongest emission. In particular, the ET efficiency from STE to Sm^{3+} in our Sb^{3+}/Sm^{3+}-codoped $Cs_2NaLuCl_6$ is higher than other Sb^{3+}/RE^{3+} codoped-DP systems (*e.g.*, Sb^{3+}/Ho^{3+}-codoped Cs_2KInCl_6 [8] and Sb^{3+}/Yb^{3+}-codoped $Cs_2AgInCl_6$ [33]) which ensures Sb^{3+}/Sm^{3+}-codoped $Cs_2NaLuCl_6$ has highly efficient Sm^{3+} emission *via* ET. The PL decay lifetime of Sb^{3+}/Sm^{3+}-codoped $Cs_2NaLuCl_6$ monitored at characteristic PL bands of Sm^{3+} show millisecond-scale lifetimes, which should be caused by the Laporte forbidden 4f-4f transitions (Fig. S10 in Supporting information) [32,34]. Moreover, the Sm^{3+} emission bands in Sb^{3+}/Sm^{3+}-codoped $Cs_2NaLuCl_6$ exhibit different decay lifetimes, which should be attributed to the emission stems from the different emission sub-energy levels of Sm^{3+} [35]. Particularly, the PL decay lifetime decreases monotonously with increasing of Sm^{3+}-doping concentration (Fig. S11 in Supporting information), which should be attributed to the increased nonradiative transition [36].

In our Sb^{3+}/Sm^{3+}-codoped system, the observed emission stems from STE and Sm^{3+} 4f-4f transitions, which makes this codoped compound has distinct excitation wavelength-dependent emission characteristics. Fig. 2e exhibits the PL spectra of 0.5%Sb^{3+}/25%Sm^{3+}-codoped $Cs_2NaLuCl_6$ under different excitation wavelengths, and the completely different spectral profiles can be seen in the visible light region, which enables this compound exhibits different emission colors. Fig. 2f shows the CIE coordinates of 0.5%Sb^{3+}/25%Sm^{3+}-codoped $Cs_2NaLuCl_6$ under various excitation wavelengths, which can change from (0.21, 0.18) under 250 nm excitation to (0.33, 0.26) under 370 nm irradiation, and the corresponding emission color turn from blue to white emission.

For a better understanding of the photophysical mechanism, the emission spectra of 0.5%Sb^{3+}/25%Sm^{3+}-codoped $Cs_2NaLuCl_6$ under various temperatures were collected in 80-400 K (Fig. 3a). Clearly, the characteristic bands of STE and Sm^{3+} emission can be witnessed in the measured temperature window (80-400 K). Fig. 3b summarizes the PL intensity under different temperatures. For the STE band in 0.5%Sb^{3+}/25%Sm^{3+}-codoped $Cs_2NaLuCl_6$, the PL intensity decreases gradually with the increase of temperature, which is similar to the phenomenon seen in 0.5%Sb^{3+}-doped $Cs_2NaLuCl_6$ (Fig. S12 in Supporting information). Moreover, the STE emission intensity in 0.5%Sb^{3+}/25%Sm^{3+}-codoped $Cs_2NaLuCl_6$ has a faster decay rate than that in 0.5%Sb^{3+}-doped $Cs_2NaLuCl_6$, which should be caused by the thermal-enhanced ET from Sb^{3+} to Sm^{3+}. In particular, the PL intensity of Sm^{3+} characteristic bands under various temperature exhibits irregular change. Generally, the thermal quenching effect will lead to the decrease of luminous intensity of STE and Sm^{3+}. However, the thermal-enhanced ET from STE to Sm^{3+} will further weaken the PL intensity of STE, but can boost the PL intensity of Sm^{3+} with increasing temperature. Under the influence of the above two factors, the PL intensity of Sm^{3+} characteristic bands show the unique PL characteristics in the temperature-dependent PL spectra, which is similar to Sb^{3+}/Ho^{3+}-codoped Cs_2KInCl_6 DP [8]. It is worth noting that when the temperature exceeds 300 K, although there is thermal-enhanced energy transfer from Sb^{3+} to Sm^{3+}, the thermal quenching dominates the emission intensity of Sm^{3+}. Therefore, when the temperature exceeds 300 K, the emission intensity of Sm^{3+} decreases gradually with increasing of temperature. The PL intensity of Sm^{3+} with

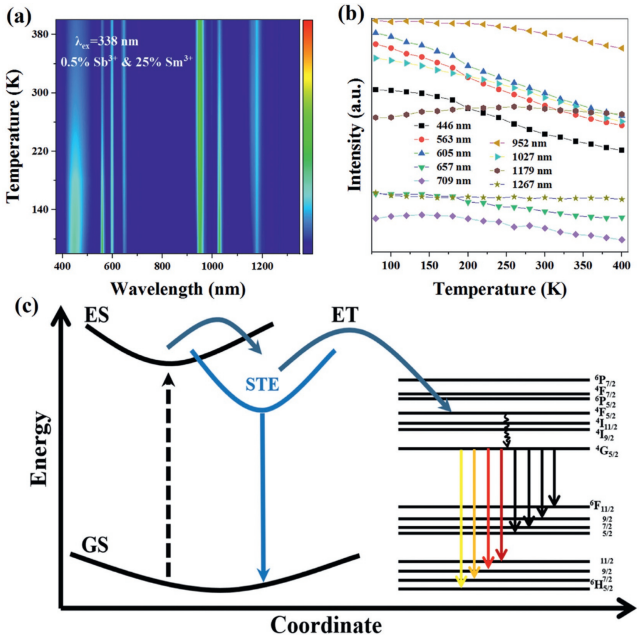

Fig. 3. Temperature-dependent PL spectra of 0.5%Sb^{3+}/25%Sm^{3+}-codoped $Cs_2NaLuCl_6$. (b) Emission intensity *versus* temperature. (c) Photophysical mechanism of Sb^{3+}/Sm^{3+}-codoped $Cs_2NaLuCl_6$.

different emission bands exhibits distinct degrees of attenuation, which can be assigned to the different sensitivity of the sub-energy levels of Sm^{3+} to temperatures.

Based on the above results, the possible photophysical mechanism of Sb^{3+}/Sm^{3+}-codoped $Cs_2NaLuCl_6$ can be summarized in Fig. 3c. Under UV photoexcitation, the electrons are excited from the ground state to the excited state. Subsequently, the excited electrons undergo the intersystem crossing from excited state to STE state due to the lattice distortion and intense electron-phonon coupling. Therefore, a broadband blue emission centered at 446 nm can be witnessed. Parallelly, the other part of electrons relaxes to the excited state of Sm^{3+} *via* the ET from STE to Sm^{3+}, and then decay to the $^4G_{5/2}$ level *via* the non-radiation transition process. Therefore, the multiple PL bands at, 563, 605, 657, 709, 952, 1027, 1179, and 1269 nm can be witnessed, which stems from the 4f-4f radiation transition of Sm^{3+} [37,38].

Moreover, the as-synthesized codoped compounds also have excellent stabilities. Taking 0.5%Sb^{3+}/20%Sm^{3+}-codoped $Cs_2NaLuCl_6$ as an example, its integral PL intensity remains basically unchanged after being stored in air for 3 months (Fig. S13 in Supporting information), and the XRD pattern exhibits an identical profile with the pristine one (Fig. S14 in Supporting information). Hence, 0.5%Sb^{3+}/20%Sm^{3+}-codoped $Cs_2NaLuCl_6$ has an outstanding chemical stability. Parallelly, the emission intensity of 0.5%Sb^{3+}/20%Sm^{3+}-codoped $Cs_2NaLuCl_6$ exhibits negligible changes after being light irradiation for 300 minutes (Fig. S15 in Supporting information), further confirming its remarkable photostability in the atmosphere.

Given the remarkable stabilities and superior optical properties of Sb^{3+}/Sm^{3+}-codoped samples, a high-performance vis/NIR-LED was fabricated *via* coating 0.5%Sb^{3+}/20%Sm^{3+}-codoped $Cs_2NaLuCl_6$ on a 315 nm UV chip. Fig. 4a shows the electroluminescence (EL) spectrum of the as-fabricated device, and the inset shows the photographs of the operating device taken by visible (left) and NIR (right) cameras. Clearly, the EL spectrum covers the entire visible and near-infrared region, which echoes well with the emission spectra of Sb^{3+}/Sm^{3+}-codoped $Cs_2NaLuCl_6$. Moreover, the as-fabricated LED has the correlated color temperature (CCT) of 8270

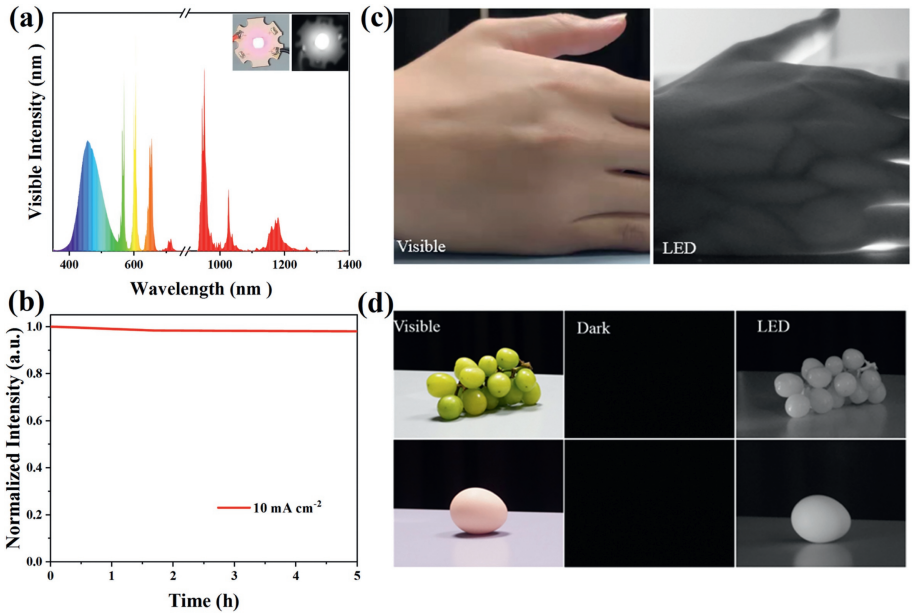

Fig. 4. (a) EL spectrum of as-fabricated 0.5%Sb^{3+}/20%Sm^{3+}-codoped $Cs_2NaLuCl_6$ based vis/NIR-LED under 315 nm chip excitation. The inset shows the optical images of the operating LED taken by visible (left) and NIR (right) cameras, respectively. (b) The long-term stability of as-fabricated device after operating for 5 hours. (c) The application of the as-fabricated device in biomedical imaging. (d) Photographs of grapes and egg illuminated by daylight and NIR-LED.

K, color rendering index (CRI) of 75.8, and CIE coordinates of (0.30, 0.28). Also noteworthy, the as-fabricated device exhibits outstanding stability, and the EL intensity remains unchanged after operating for 5 h under 10 mA drive current (Fig. 4b). As we know, the NIR light has enormous application potential in biomedical imaging for its strong penetration, non-invasively, high resolution, and so forth. Thus, we demonstrated the application of the device in biomedical imaging in further proof-of-concept experiment. As shown in Fig. 4c, the palm in the daylight can be captured by the visible camera clearly. Since different tissues have different absorption for the NIR light, thus the distribution of veins in the palm can be captured clearly by the NIR camera when the as-fabricated LED starts to operate (Fig. 4c, right). In addition, the optical images of grapes and egg are taken by a visible camera under daylight (Fig. 4d, left), and nothing can be observed in the dark environment (Fig. 4d, middle). In particular, the black-and-white images of the grapes and egg can be witnessed when the LED was tuned on (Fig. 4d, right). Hence, the above results illustrate that the as-fabricated LED has great application potential in biomedical imaging and night vision.

Recently, lead-free metal halides with unique PL characteristics have drawn much attentions in the field of smart photonics [39–44]. In our system, Sb^{3+}/Sm^{3+}-codoped $Cs_2NaLuCl_6$ exhibits broad emission that can cover visible light range and NIR light region, and has tunable emission color under different excitation wavelengths. This unique photophysical properties enable us to demonstrate its application in triple-mode fluorescence anti-counterfeiting and information encryption under different external stimuli. As illustrated in Fig. 5a, the alphabet of "X" was fabricated *via* filling Sb^{3+}/Sm^{3+}-codoped $Cs_2NaLuCl_6$ powders into the customized pattern templates. Upon 254 nm irradiation, the pattern "X" exhibits blue emission, and further change into white emission under 365 nm excitation. Particularly, when a 700 nm cutoff filter is added, the visible light is removed. Thus, the "X" pattern with NIR emission can be recorded by the NIR camera, and the triple-mode fluorescence anti-counterfeiting is realized based on Sb^{3+}/Sm^{3+}-codoped $Cs_2NaLuCl_6$ under different external stimuli. In order to further improve the diversity of fluorescent anti-counterfeiting, we fabricated a new pattern of "8" by combining Sb^{3+}-doped $Cs_2NaLuCl_6$ and Sb^{3+}/Sm^{3+}-codoped $Cs_2NaLuCl_6$. As shown in Fig. 5b, the pattern "8" emits blue emission under 254 nm radiation. When the excitation wavelength is 365 nm, the number of "1" made by Sb^{3+}-doped $Cs_2NaLuCl_6$ exhibits blue emission, and the number of "3" made by Sb^{3+}/Sm^{3+}-codoped $Cs_2NaLuCl_6$ shines white emission. Interestingly, with a 700 nm cutoff filter, the number "3" with NIR emission can be captured by the NIR camera. Subsequently, we further demonstrated the application of as-synthesized samples in multiple information encryption. As shown in Fig. 5c, we fabricated a PL dot array based on the combination of Sb^{3+}-doped $Cs_2NaLuCl_6$ and Sb^{3+}/Sm^{3+}-codoped $Cs_2NaLuCl_6$. To be more specific, the Sb^{3+}-doped $Cs_2NaLuCl_6$ is filled into the first line of the PL dot array, while the rest is filled

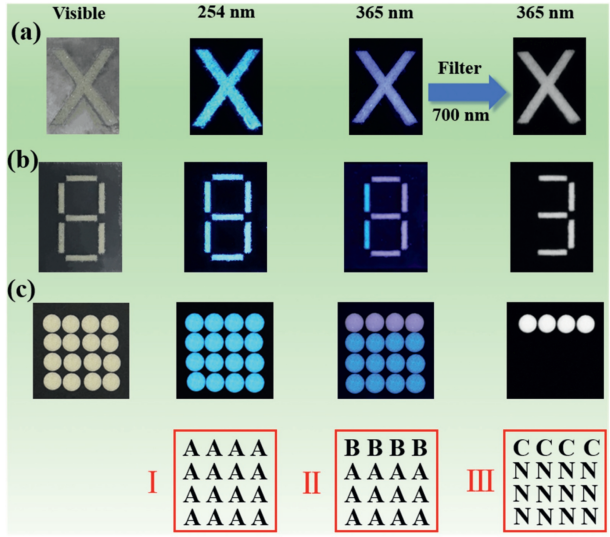

Fig. 5. (a) Optical image of "X" pattern made by Sb^{3+}/Sm^{3+}-codoped $Cs_2NaLuCl_6$. (b) Optical image of the number "8" made by Sb^{3+}-doped $Cs_2NaLuCl_6$ and Sb^{3+}/Sm^{3+}-codoped $Cs_2NaLuCl_6$. (c) Photographs of PL dot array made by Sb^{3+}/Sm^{3+}-codoped $Cs_2NaLuCl_6$ (first line) and Sb^{3+}-doped $Cs_2NaLuCl_6$ (second, third, and fourth lines).

with Sb^{3+}/Sm^{3+}-codoped $Cs_2NaLuCl_6$. Moreover, the blue point represents "A", the white point represents "B", the NIR point represents "C", and the non-emission represents "N". Hence, the detailed information encryption processes are given as follows: Under 254 nm excitation, all the PL dots exhibit blue emission, thus the Information I can be obtained. When the whole PL dot array is irradiated by 365 nm, the Information II can be transmitted, in which the blue dots on the first line and the white dots on the other position. Moreover, the PL dots with NIR emission on the first line can be captured by the NIR camera, and other position exhibit non-emission, resulting in the Information III. Notably, this multiple dynamic luminescence reported in our work under different external stimuli can apply more information encryption scenarios, thus greatly improving information security.

In summary, we synthesized Sb^{3+}/Sm^{3+}-codoped rare earth-based double perovskite $Cs_2NaLuCl_6$, and the obtained emission spectra can cover both visible light and NIR light regions, which stems from dopant induced STE emission and Sm^{3+} emission, respectively. The photophysical processes of Sb^{3+}/Sm^{3+}-codoped $Cs_2NaLuCl_6$ were discussed through steady-state/transient PL spectra and temperature-dependent PL spectra. The results show that Sb^{3+} can work as the sensitizer to enhance Sm^{3+} emission *via* ET from STE to Sm^{3+}. Moreover, the similar ionic activity between Lu^{3+} and Sm^{3+} enables more Sm^{3+} doped into the host lattice. Thus, the efficient visible and NIR emission in Sb^{3+}/Sm^{3+}-codoped $Cs_2NaLuCl_6$ with PLQY of 74.58% and 23.12% can be obtained. Parallelly, the tunable emission characteristics of Sb^{3+}/Sm^{3+}-codoped $Cs_2NaLuCl_6$ were demonstrated in the visible light range, which can be tuned from blue (254 nm excitation) to white emission (365 nm excitation). Moreover, the visible emission can be removed through a 700 nm cut-off filter, and only the NIR emission can be captured by the NIR camera. Considering the remarkable stability and unique photophysical properties, we further demonstrated the application of Sb^{3+}/Sm^{3+}-codoped $Cs_2NaLuCl_6$ in high-performance NIR LED, triple-mode fluorescence anti-counterfeiting and information encryption. These findings provide deep insights for the further application of rare earth-based double perovskite in optoelectronic devices.

Declaration of competing interest

The authors declare that they have no known competing financial interests or personal relationships that could have appeared to influence the work reported in this paper.

Acknowledgments

The authors thank the Scientific and Technological Bases and Talents of Guangxi (Nos. Guike AD23026119, AD21238027), the Guangxi National Science Fundation Project (No. 2020GXNSFDA238004) and the "Guangxi Bagui Scholars" foundation for financial support.

Supplementary materials

Supplementary material associated with this article can be found, in the online version, at doi:10.1016/j.cclet.2023.109462.

References

[1] Z. Chen, Q. Wang, Y. Tong, et al., J. Phys. Chem. Lett. 13 (2022) 4701–4709.
[2] C.Y. Zhong, L. Xiao, J. Zhou, et al., Chem. Eng. J. 431 (2022) 134110.
[3] T. Milstein, D. Kroupa, D. Gamelin, Nano Lett. 18 (2018) 3792–3799.
[4] Y. Liu, M.S. Molokeev, Z. Xia, Energy Mater Adv. 2021 (2021) 2585274.
[5] A. Zhang, Y. Liu, G. Liu, et al., Chem. Mater. 34 (2022) 3006–3012.
[6] Y. Liu, A. Nag, L. Manna, et al., Angew. Chem. Int. Ed. 60 (2021) 11592–11603.
[7] Y. Mahor, W. Mir, A. Nag, J. Phys. Chem. C 13 (2019) 15787–15793.
[8] W. Huang, H. Peng, Q. Wei, et al., Adv. Opt. Mater. 11 (2023) 2203103.
[9] X. Li, D. Wang, Y. Zhong, et al., Adv. Sci. 10 (2023) 2207571.
[10] S. Ji, R. Li, H. Huang, et al., Light Sci. Appl. 11 (2022) 52.
[11] Y. Liu, X. Rong, M. Li, et al., Angew. Chem. Int. Ed. 59 (2020) 11634–11640.
[12] H. Arfin, J. Kaur, T. Sheikh, et al., Angew. Chem. Int. Ed. 59 (2020) 11307–11311.
[13] S. Saikia, A. Joshi, H. Arfin, et al., Angew. Chem. Int. Ed. 61 (2022) e202201628.
[14] Y. Wang, S. Bai, J. Sun, et al., J. Alloys Compd. 947 (2023) 169602.
[15] W. Gan, L. Cao, S. Gu, et al., Chem. Mater. 35 (2023) 5291–5299.
[16] N. Liu, W. Zheng, R. Sun, et al., Adv. Funct. Mater. 32 (2022) 2110663.
[17] E. Cui, X. Yuan, L. Tang, et al., Appl. Surf. Sci. 609 (2023) 155472.
[18] W. Gan, B.M. Liu, L. Huang, et al., Adv. Opt. Mater. 10 (2022) 2102851.
[19] G. Zhang, P. Dang, L. Tian, et al., Adv. Opt. Mater. 11 (2023) 2202369.
[20] Y. Chen, L. Zhou, S. Zhou, et al., Inorg. Chem. 62 (2023) 2806–2816.
[21] H. Peng, S. Yao, Y. Guo, et al., J. Phys. Chem. Lett. 11 (2020) 4703–4710.
[22] B. Yang, K. Han, J. Phys. Chem. Lett. 12 (2021) 8256–8262.
[23] H. Peng, B. Zou, J. Phys. Chem. Lett. 13 (2022) 1752–1764.
[24] J. Sun, W. Zheng, P. Huang, et al., Angew. Chem. Int. Ed. 61 (2022) e202201993.
[25] X. He, H. Peng, Q. Wei, et al., Aggregate (2023) e407.
[26] S. Ge, H. Peng, Q. Wei, Adv. Opt. Mater. 11 (2023) 2300323.
[27] Y. Wang, S. Bai, J. Sun, et al., J. Alloy. Compd. 934 (2023) 167952.
[28] F. Locardi, E. Gianotti, I. Nelli, et al., Mater. Res. Bull. 86 (2017) 220–227.
[29] H. Peng, Y. Tian, Z. Yu, et al., Sci. China Mater. 65 (2022) 1594–1600.
[30] J. Ni, B. Zhou, S. Fang, Chem. Mater. 34 (2022) 6288–6295.
[31] S. Li, Q. Hu, J. Luo, et al., Adv. Opt. Mater. 7 (2019) 1901098.
[32] J. Nie, H. Li, S. Fan, et al., Cell Rep. Phys. Sci. 3 (2022) 100820.
[33] L. Cao, X. Jia, W. Gan, et al., Adv. Funct. Mater. 33 (2023) 2212135.
[34] W. Yang, P. Dang, G. Zhang, et al., Adv. Opt. Mater. 11 (2023) 2300468.
[35] P. Dang, Z. Zhang, W. Yang, et al., Chem. Mater. 35 (2023) 1640–1650.
[36] B. Su, M. Li, E. Song, et al., Adv. Funct. Mater. 31 (2021) 2105316.
[37] C. Chen, M. Jin, J. Xiang, et al., Ceram. Int. 49 (2023) 25232–25239.
[38] S. Han, D. Tu, Z. Xie, et al., Adv. Sci. 9 (2022) 2203735.
[39] S. Feng, Y. Ma, S. Wang, et al., Angew. Chem. Int. Ed. 134 (2022) e202116511.
[40] B. Zhou, G. Xiao, D. Yan, Adv. Mater. 33 (2021) e2007571.
[41] B. Zhou, D. Yan, Adv. Funct. Mater. 33 (2023) 2300735.
[42] Y.J. Ma, G. Xiao, X. Fang, et al., Angew. Chem. Int. Ed. 62 (2023) e202217054.
[43] S. Liu, Y. Lin, D. Yan, Sci. Bull. 67 (2022) 2076.
[44] F. Nie, B. Zhou, K.Z. Wang, et al., Chem. Eng. J. 430 (2022) 133084.